

This is the accepted manuscript made available via CHORUS. The article has been published as:

Antiferromagnetism and the emergence of frustration in the sawtooth lattice chalcogenide olivines

$\text{Mn}_{\{2\}}\text{SiS}_{\{4-x\}}\text{Se}_{\{x\}}$ ($x=0-4$)

H. Nhalil, R. Baral, B. O. Khamala, A. Cosio, S. R. Singamaneni, M. Fitta, D. Antonio, K. Gofryk, R. R. Zope, T. Baruah, B. Saparov, and H. S. Nair

Phys. Rev. B **99**, 184434 — Published 24 May 2019

DOI: [10.1103/PhysRevB.99.184434](https://doi.org/10.1103/PhysRevB.99.184434)

Antiferromagnetism and the emergence of frustration in saw-tooth lattice chalcogenide olivines



H. Nhalil,¹ R. Baral,² B. O. Khamala,² A. Cosio,² S. R. Singamaneni,² M. Fitta,³
D. Antonio,⁴ K. Gofryk,⁴ R. R. Zope,² T. Baruah,² B. Saparov,^{1,*} and H. S. Nair^{2,†}

¹*Department of Chemistry and Biochemistry, University of Oklahoma, 101 Stephenson Parkway, Norman, OK 73019, USA*

²*Department of Physics, 500 W University Ave, University of Texas at El Paso, El Paso, TX 79968, USA*

³*Institute of Nuclear Physics, Polish Academy of Sciences, 31-342 Kraków, Poland*

⁴*Idaho National Laboratory, Idaho Falls, ID 83415, USA*

(Dated: May 6, 2019)

The magnetism in the saw-tooth lattice of Mn in the olivine chalcogenides, $\text{Mn}_2\text{SiS}_{4-x}\text{Se}_x$ ($x = 1-4$) is studied in detail by analyzing their magnetization, specific heat and thermal conductivity properties and complemented with density functional theory calculations. The air-stable chalcogenides are antiferromagnets and show a linear trend in the transition temperature, T_N as a function of Se-content (x) which shows a decrease from $T_N \approx 86$ K for Mn_2SiS_4 to 66 K for Mn_2SiSe_4 . Additional new magnetic anomalies are revealed at low temperatures for all the compositions. Magnetization irreversibilities are observed as a function of x . The specific heat and the magnetic entropy indicate the presence of short-range spin fluctuations in $\text{Mn}_2\text{SiS}_{4-x}\text{Se}_x$. A spin-flop antiferromagnetic phase transition in the presence of applied magnetic field is present in $\text{Mn}_2\text{SiS}_{4-x}\text{Se}_x$, where the critical field for the spin flop increases from $x = 0$ towards 4 in a non-linear fashion. Density functional theory calculations show that an overall antiferromagnetic structure with ferromagnetic coupling of the spins in the ab -plane minimizes the total energy. The band structures calculated for Mn_2SiS_4 and Mn_2SiSe_4 reveal features near the band edges similar to those reported for Fe-based olivines suggested as thermoelectrics; however the experimentally determined thermal transport data do not support superior thermoelectric features. The transition from long-range magnetic order in Mn_2SiS_4 to short-range order and spin fluctuations in Mn_2SiSe_4 is explained using the variation of the Mn-Mn distances in the triangle units that constitutes the saw-tooth lattice upon progressive replacement of sulphur with selenium. **Overall, the results presented here point towards the role played by magnetic anisotropy and geometric frustration in the antiferromagnetic state of the saw-tooth olivines.**

I. INTRODUCTION

Complex magnetic excitations from frustrated lattices of magnetic atoms is an attractive topic in quantum correlated systems. The saw-tooth antiferromagnetic chain has a frustrated topology of corner-sharing triangles of spins where the ground state of the spin-half saw-tooth chain is understood exactly¹⁻³. Variety of ground states are predicted for the saw-tooth lattice depending on the ratio of the exchange interaction strengths between the base-base and the base-vertex pairs⁴⁻⁸. The saw-tooth systems attain importance in connection with the zero energy flat-band modes similar to the case of Kagome lattices^{9,10} and are valuable as potential materials for magnonics¹¹. Experimental studies on saw-tooth lattices are limited in number; some examples are the delafossites, olivine and germanates¹²⁻¹⁵. In this connection, chalcogenide olivines have received less attention regarding the magnetism and magnetic excitations arising from their underlying saw-tooth lattice. The A_2BX_4 ($A = \text{Mn, Fe, Ni}$; $B = \text{Si, Ge}$; $X = \text{S, Se, Te, O}$) olivines, where the A atoms form a saw-tooth lattice, are well-known semiconducting magnetic compounds which find applications in optoelectronics and magnetic devices^{16,17}. They have been recently computationally projected as suitable thermoelectric candidates owing to peculiar band structure features¹⁸. They crystallize in orthorhombic $Pnma$ space group and have relatively small tetrahedral ions (B) and large octahedral ions (A). Olivines have a spinel-like structure but uses one quadrivalent and two divalent cations $A_2^{2+}B^{4+}X_4$ instead of

two trivalent and one divalent cations. The A sites consist of the two crystallographically independent sites ($4a$ and $4c$ sites) and form a triangle-based saw-tooth chain structure through the edge-sharing bonds along the b -axis¹⁹. Due to this structural feature, the A -site lattice is geometrically frustrated when it is occupied by magnetic ions¹⁹. The end-compounds of $\text{Mn}_2\text{SiS}_{4-x}\text{Se}_x$ – Mn_2SiS_4 and Mn_2SiSe_4 – order antiferromagnetically below their Néel temperature, $T_N \approx 83$ K and 66 K, respectively²⁰⁻²³. Mn_2SiS_4 belongs to the class of anisotropic uniaxial antiferromagnets but with anomalous magnetic features near the spin-flop transition²⁰. A weak ferromagnetic interaction exists in a narrow temperature window between 83 K and 86 K, while displaying uniaxial anisotropy with the b -direction as the easy axis. The origin of weak ferromagnetism (WF) and the unusual temperature dependence of spin-flop critical field is unclear in olivines despite the microscopic origin of WF which is supported by neutron scattering experiments²⁴. At 4.2 K a collinear ferromagnetic arrangement of the Mn spins at the two distinct crystallographic positions, $4a$ (a site with inversion) and $4c$ (mirror), was observed along the b axis. As the temperature increases to 83 K, the orientation of the $4a$ spins turns in the ab plane. At 83 K, both the $4a$ and the $4c$ spins reorient along the a axis but with some canting in the ac plane. It is in the very small temperature range of 83–86 K, spins at two different crystallographic positions display weak ferromagnetism. The paramagnetic to antiferromagnetic transition has been identified as belonging to the Heisenberg universality class and the weak ferromagnetic transition as

first order with a latent heat ≈ 0.01 J/mol²⁵. A very low value of magnetic entropy, about 5% of $R\ln(2S + 1)$, is found to be released at the antiferromagnetic transition, indicating that the spin entropy is not completely removed at the T_N . Experimental support for the short-range spin fluctuations come from the fact that purely magnetic intensity was observed in neutron diffraction data up to 140 K²⁴.

On the other end of the composition series of $\text{Mn}_2\text{SiS}_{4-x}\text{Se}_x$ is the case of Mn_2SiSe_4 , which has the magnetic easy axis along crystallographic c -direction of the orthorhombic cell²³. In the case of Mn_2SiSe_4 , the average magnetic structure remains in a configuration intermediate to a ferrimagnet and an antiferromagnet for most of the $T < T_N$ region. Though both Mn_2SiS_4 and Mn_2SiSe_4 are reported to show similar magnitude of magnetization, Mn_2SiSe_4 displays pronounced field and temperature cycling dependencies in magnetic susceptibility²³. The temperature range spanned by the magnetization maximum (between 66 K and 17 K, almost 50 K) is much wider compared to that of Mn_2SiS_4 (between 86 K and 83 K, approximately 3 K)^{22,23}. The broadness of the transition in magnetic susceptibility of Mn_2SiSe_4 and the hysteresis-like effects already suggests strongly competing interactions leading to a frustrated magnetic state. An interesting aspect of the olivines that has recently received attention is related to thermoelectricity. Quasi-flat band edges near the valence and conduction bands were predicted using density functional theory calculations in the case of Fe_2GaCh_4 ($Ch = \text{S}, \text{Se}, \text{Te}$)¹⁸. This theoretical investigation was preceded by experiments that showed nano-structured Fe_2GeS_4 is a photovoltaic material^{16,26}. Experimental studies have shown that Fe_2SiS_4 and Fe_2GeS_4 possess significant thermopower²⁷.

In the present paper we undertake a detailed experimental study of magnetism in $\text{Mn}_2\text{SiS}_{4-x}\text{Se}_x$. Our research is motivated by the prospect of understanding the role of magnetic frustration in the saw-tooth lattice of Mn in the series of olivines as the transition metal environment is altered from sulfur-rich to selenium-rich. A detailed magnetic and thermal property investigation of $\text{Mn}_2\text{SiS}_{4-x}\text{Se}_x$ ($x = 0, 1, 2, 3, 4$) solid solutions is undertaken and is complemented with density functional theory calculations.

II. METHODS

A. Experimental techniques

Elemental Mn, Si, S and Se (99.99%, Aldrich) were used as reactants to synthesize $\text{Mn}_2\text{SiS}_{4-x}\text{Se}_x$, $x = 0-4$. Stoichiometric amount of these elements were weighed and mixed properly using a mortar and pestle before pelleting and loading into a 10 mm diameter quartz ampule in a N_2 -filled glove box. The quartz tubes were flame-sealed under a dynamic vacuum with pressure less than 10^{-3} mTorr. The reaction mixtures were heated at 1000°C for 24 hours then cooled to room temperature at a rate of 100°C/h. To improve the phase purity and crystallinity, samples were re-ground, pelleted and annealed under identical conditions as necessary. Room temperature

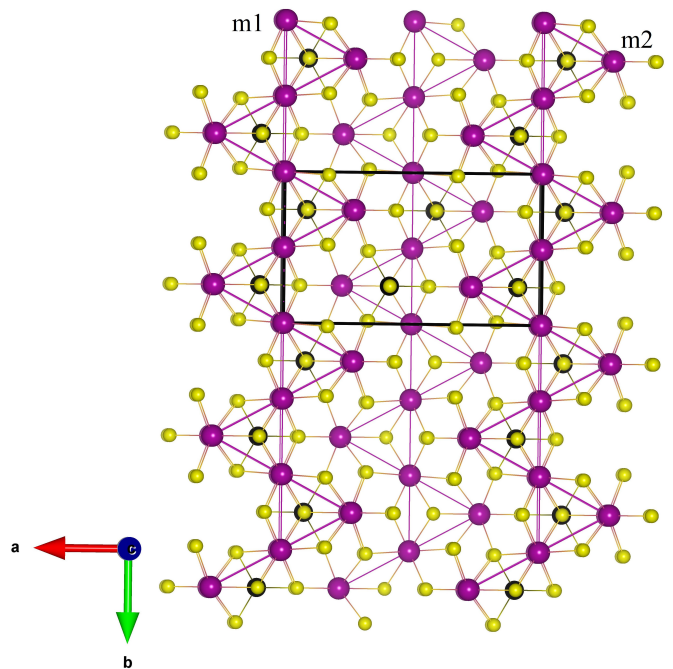


FIG. 1. (color online) A schematic of the olivine structure of Mn_2SiS_4 . The unit cell is outlined in black solid line. The purple spheres are Mn. The saw-tooth lattice formed by Mn^{2+} at the two crystallographically-inequivalent sites, m_1 and m_2 is shown. The line of m_1 atoms forms along the b direction. In the figure, the black spheres are Si, and the yellow are S. The figure was created using VESTA²⁸.

powder X-ray diffraction (PXRD) measurements were performed on a Rigaku MiniFlex600 instrument with a D/tex detector using a Ni-filtered $\text{Cu-K}\alpha$ radiation ($\lambda_1: 1.540562$ Å; $\lambda_2: 1.544398$ Å). X-ray data collection experiments were performed at room temperature in the $10-70^\circ$ (2θ) range, with a step size of 0.02° . Data analysis was performed using Rigaku PDXL software package. The collected data were fitted using the decomposition method (Pawley fitting) embedded in the PDXL package. For air stability studies, powder samples of all three compositions were left in ambient air for a period of 6 weeks. PXRD measurements were regularly performed during this period using the conditions described above. The specific heat, $C_p(T)$, of the samples were measured using the heat pulse method in a commercial VersaLab, Physical Property Measurement System from Quantum Design. Tiny pellets of $\text{Mn}_2\text{SiS}_{4-x}\text{Se}_x$ of mass approximately 2-3 mg were used for the measurements. The sample was attached to the calorimeter puck using N Apiezon grease. The $C_p(T)$ was measured in the temperature range 50 K–300 K under 0 T and 3 T. The temperature and field-dependent magnetization measurements were performed in a SQUID Magnetic Property Measurement System. DC magnetization was measured in the temperature range 2–300 K and isothermal magnetization at 2 K in the range -7 T to 7 T. The thermal conductivity was measured using the TTO option in a commercial DynaCool-9, Physical Property Measurement System from Quantum Design.

TABLE I. The lattice parameters and the goodness-of-fit parameter (R_{wp}) and the χ^2 for the $\text{Mn}_2\text{SiS}_{4-x}\text{Se}_x$ compounds at 300 K. All compositions crystallize in the orthorhombic $Pbnm$ space group.

	a (Å)	b (Å)	c (Å)	R_{wp}	χ^2
Mn_2SiS_4	12.692(9)	7.435(3)	5.941(3)	3.94%	2.89
$\text{Mn}_2\text{SiS}_3\text{Se}$	12.860(1)	7.527(4)	6.009(8)	2.48	1.23
$\text{Mn}_2\text{SiS}_2\text{Se}_2$	13.000(3)	7.605(6)	6.076(5)	2.31	1.42
$\text{Mn}_2\text{SiSSe}_3$	13.150(8)	7.690(9)	6.156(1)	1.78	1.35
Mn_2SiSe_4	13.302(8)	7.777(2)	6.243(6)	1.97	1.4

	$d_{\text{Mn-S}}$ (Å)	$d_{\text{Si-S}}$ (Å)	$d_{\text{Mn-Mn}}$ (Å)
Mn_2SiS_4	2.5616(4)	2.193(4)	$3.9112(3) \times 2$
	2.6391(5)	2.0375(3)	3.7169(6)
	2.6226(5)		4.787(9) (along c)
Mn_2SiSe_4	2.7034(4)	2.298(4)	$4.0997(5) \times 2$
	2.7513(1)	2.3118(6)	3.8876(4)
	2.7403(9)		4.7153(6) (along c)

B. Computational methods

The density functional theory (DFT) calculations were carried out using the Vienna ab initio simulation package (VASP)^{29–32}. The projector augmented wave (PAW) method was utilized for the electron-ion interaction^{33–35} with an en-

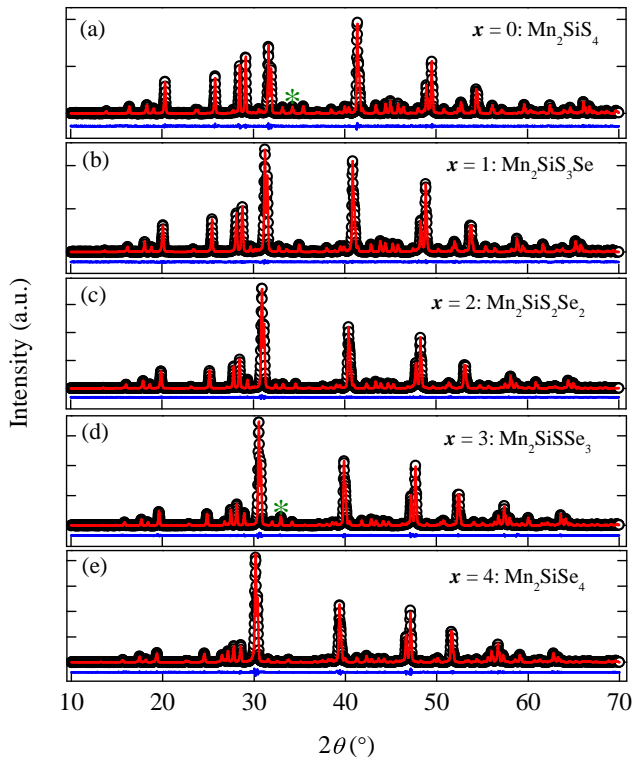


FIG. 2. (color online) (a-e) The PXRD patterns of $\text{Mn}_2\text{SiS}_{4-x}\text{Se}_x$ ($x = 0-4$) compositions are presented along with the results of structural analysis using $Pbnm$ space group. The black markers represent experimental data and the red lines are the fit using Le Bail approach. The blue horizontal line shows the difference curve. In (a) and (d), an asterisk marks a minor impurity phase, α -MnS ($\approx 2\text{wt}\%$).

ergy cutoff of 470 eV for the plane-wave basis functions. The generalized gradient approximation to exchange-correlation functional by Perdew, Burke, and Ernzhofers³⁶ was used. A Γ -centered ($4 \times 4 \times 4$) k -point grid based on Monkhorst-Pack scheme³⁷ was employed for initial structure optimization and later a finer grid of $6 \times 11 \times 13$ was used for further refinement. We have relaxed the structures until the Hellmann-Feynman forces on the ions were lower than $0.04 \text{ eV}/\text{\AA}$. An initial spin moment of $5 \mu_B$ to Mn ions were assigned and the spin moment was allowed to relax. We also used VESTA²⁸ software package for generating the crystal structures.

III. RESULTS AND DISCUSSION

A. X ray diffraction and air stability

Powder X-ray diffraction (PXRD) patterns along with the Pawley fitting of $\text{Mn}_2\text{SiS}_{4-x}\text{Se}_x$ ($x = 0-4$) compounds measured at room temperature are shown in Fig 2. The results of the structural analysis of the PXRD patterns are summarized in Table (I). All samples crystallize in the orthorhombic $Pbnm$ space group (# 62). The compounds, $\text{Mn}_2\text{SiS}_3\text{Se}$ ($x = 1$), $\text{Mn}_2\text{SiS}_2\text{Se}_2$ ($x = 2$), and Mn_2SiSe_4 ($x = 4$) were obtained as pure phase samples, whereas the Mn_2SiS_4 ($x = 0$) and $\text{Mn}_2\text{SiSSe}_3$ ($x = 3$) samples contained minor impurity phase of α -MnS quantified to be less than 2 wt%.

Air stability of $\text{Mn}_2\text{SiS}_{4-x}\text{Se}_x$ is very important feature while considering use in practical device applications. Being a non-oxide, many chalcogenide based materials are prone to degradation upon exposure to air and moisture^{38–40}. Air stability of $\text{Mn}_2\text{SiS}_{4-x}\text{Se}_x$ compounds were investigated for over a period of 6 weeks by keeping the powder sample exposed to the ambient atmosphere. PXRD was collected regularly during this period and analyzed. PXRD patterns of the as-synthesized samples and those of the samples after exposure to air for 6 weeks showed no appreciable differences (not shown). After 6-weeks exposure to air, no additional peaks or peak broadening was observed in any of the five compositions. We confirm that Mn_2SiSe_4 series have good air stability thereby establishing their potential for use in practical applications.

The important structural feature of the $\text{Mn}_2\text{SiS}_{4-x}\text{Se}_x$ compounds from the perspective of magnetism is the saw-tooth like triangular arrangement of Mn lattice.¹⁹ Such a lattice forms the basis for a frustrated lattice depending on the different bond lengths or the exchange parameters related to the triangular motif building up the saw tooth. Mn has two crystallographically distinct positions in this structure, *viz.*, $4a$ and $4c$ where there are four magnetic ions per cell with inversion symmetry and mirror symmetry respectively. Previous neutron powder diffraction studies on the $x = 0$ compound in the temperature range 4.2 K–300 K have shown that there is no structural change in the temperature range mentioned above. For all the $\text{Mn}_2\text{SiS}_{4-x}\text{Se}_x$ compounds, we assume the olivine structure in the entire temperature range employed in the present study. The refined lattice parameters that we obtain in the present study for Mn_2SiSe_4 match well with the

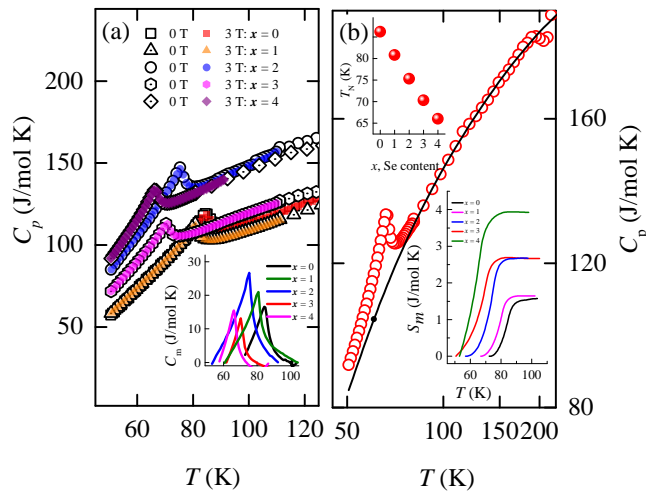


FIG. 3. (color online) (a) The specific heat of $\text{Mn}_2\text{Si}_{4-x}\text{Se}_x$ ($x = 0-4$) obtained in 0 T and 3 T are plotted together, showing no significant influence of the external magnetic field on the T_N s. (b) Shows the $C_p(T)$ of Mn_2Si_4 (red circles) along with the curve fit using Einstein model (solid line). The inset of (a) shows the magnetic specific heat, C_m . The top inset in (b) shows that, with increasing x , the T_N decreases from 86 K to 66 K while the entropy, S_m , is shown in the bottom inset. Significantly low value of entropy compared to $R \ln(2S+1)$ is released at the magnetic transition in $\text{Mn}_2\text{Si}_{4-x}\text{Se}_x$ chalcogenides.

earlier report on the crystal structure.⁴¹ Incidentally, a structural peculiarity that the Mn(1) octahedra being less distorted than the Mn(2) octahedra was mentioned in Ref[41]. Similarly the lattice parameters obtained for Mn_2SiSe_4 series in the present work also matches well with the reported values.²²

B. Specific heat

The experimentally measured specific heat of $\text{Mn}_2\text{Si}_{4-x}\text{Se}_x$ ($x = 0-4$) are presented in Fig 3 (a) where the specific heat under 0 T and 3 T are plotted together. The parent composition, Mn_2Si_4 reproduces the antiferromagnetic phase transition at $T_N \approx 84$ K^{20,25,42,43} which characterizes the paramagnetic-to- antiferromagnetic phase transition. It is reported that in the temperature range 83 K–86 K, Mn_2Si_4 displays WF; further, below 83 K it is an antiferromagnet. From the present $C_p(T)$ data of Mn_2Si_4 , we identify the AF transition at 86.2 K by taking the derivative, $dC_p(T)/dT$. The WF transition reported at 83 K is less-conspicuous in our derivative plot (not shown). Under the application of 3 T magnetic field, no changes to the peak at T_N is noticeable for any of the compositions $x = 0$ to 4. This points towards strong AF nature of the underlying spin structure, up to atleast 3 T. Upon substituting S with Se, the transition temperature T_N decreases from 86 K for $x = 0$ to 66 K for $x = 4$, Mn_2SiSe_4 . The evolution of the T_N as a function of x is presented in the inset (b) of Fig 3.

In order to account for the phonon part of the specific heat of $\text{Mn}_2\text{Si}_{4-x}\text{Se}_x$, an Einstein model-based curve fit

was administered to the $C_p(T)$. We have used two separate Einstein terms and such a fit is demonstrated in Fig 3 (b) for the case of Mn_2Si_4 . In (b), the solid line represents the fit using the following expression:

$$C_{\text{Einstein}} = 3rR \sum_i a_i [x_i^2 e^{x_i} / (e^{x_i} - 1)^2] \quad (1)$$

where, $x_i = \hbar\omega_E/k_B T$ and a_i is the weight factor for each mode. The specific heat data in the temperature range, $T > 100$ K was used for the fit. We obtain the Einstein temperatures as $\theta_{E1} = 744$ K and $\theta_{E2} = 128$ K. The lattice part of the specific heat thus obtained was subtracted from the total specific heat to obtain the magnetic part, C_m which is plotted in the inset of Fig 3 (a) for all the compositions of $\text{Mn}_2\text{Si}_{4-x}\text{Se}_x$. The magnetic entropy, $S_m = \int (dC_m/T) dT$ is calculated and plotted in the inset of Fig 3 (b) for $x = 0-4$. Though the $\text{Mn}_2\text{Si}_{4-x}\text{Se}_x$ compounds undergo a PM-AF second order phase transition, it can be seen that significantly low magnetic entropy is released at the T_N . The Mn^{2+} with spin $S = 5/2$ contributes $R \ln(6) = 14.8$ J/mol-K towards spin entropy. In the case of Mn_2Si_4 , only 14% of this value is released at the T_N . This, in turn, suggests that the Mn^{2+} spins of $\text{Mn}_2\text{Si}_{4-x}\text{Se}_x$, which form a two-dimensional saw-tooth-like triangular arrangement are indeed in a frustrated magnetic state. Hence significant short-range magnetic order is expected to coexist along with the prominent AF order. It is noted here that the specific heat analysis that we have performed is on the data limited to only 50 K. Hence a comprehensive estimation of the lattice specific heat including a Debye term and extending down to low temperature was not possible. This would have resulted in a deviation in the values of S_m presented here. However, we obtain supporting values from the earlier reports on the specific heat analysis and magnetic entropy determination of Mn_2Si_4 .²⁵

C. Magnetization

The dc magnetic susceptibility, $\chi_{\text{dc}}^{\text{fc}}(T)$, of the Mn_2SiSe_4 series measured in an applied magnetic field of 500 Oe are presented in Fig 4 for $x = 0, 1, 4$ in panel (a) and $x = 2, 3$ in (b). Though the phase transition temperatures (T_N) identified in the specific heat data are reflected in magnetic susceptibility as well, a significant difference in the magnitude of magnetic susceptibility is observed for the two sets of compositions in the panels (a) and (b). The magnetic phase transition in the case of Mn_2Si_4 occurs as a sharp anomalous peak at $T_N = 83.7$ K and matches with the reported value.^{24,25} Upon progressive replacement of S with Se, the peak at the phase transition is weakened, and eventually for Mn_2SiSe_4 a very broad feature is seen below ≈ 65 K. This observation also matches with the previous report of the magnetic behaviour of Mn_2SiSe_4 .²² The linear trend of decrease in the T_N can be connected to the covalent radius difference between S (1.05 Å) and Se (1.20 Å)⁴⁴.

The inset of (a) shows the T_N values estimated from the $\chi_{\text{dc}}^{\text{fc}}(T)$ data by taking the derivative, $d\chi_{\text{dc}}^{\text{fc}}(T)/dT$. The derivative, dM/dT as a function of temperature for $x = 0-4$ are

TABLE II. The magnetic transition temperatures (T_N), effective paramagnetic moment (μ_{eff}), Curie-Weiss temperature (θ_{cw}) of different compositions of the $\text{Mn}_2\text{SiS}_{4-x}\text{Se}_x$ compounds. The T_N 's are determined from the derivative of magnetic susceptibility.

	T_N (K)	T_2 (K)	T_3 (K)	μ_{eff} (μ_B/Mn)	θ_{cw} (K)	f $ \theta_{cw}/T_N $	T_N/θ_{cw}	T_2/θ_{cw}	T_3/θ_{cw}
Mn_2SiS_4	83.7	11.7		4.0(3)	-226	2.7	0.36	0.05	
$\text{Mn}_2\text{SiS}_3\text{Se}$	81.9	11.7		4.07(2)	-221	2.7	0.36	0.05	
$\text{Mn}_2\text{SiS}_2\text{Se}_2$	77.7	19	5	3.95(5)	-219	2.8	0.35	0.08	0.02
$\text{Mn}_2\text{SiSSe}_3$	71.7	17	3.8	3.8(2)	-193	2.7	0.36	0.08	0.02
Mn_2SiSe_4	65.5	13.7		5.9(4)	-336	5.2	0.19	0.04	

presented in the panels (c) to (g). The magnetic transition temperatures, T_N 's, thus estimated through the derivatives are collected in Table II. From the magnetization data, we have been able to identify multiple magnetic anomalies at low temperatures for all the compositions in $\text{Mn}_2\text{SiS}_{4-x}\text{Se}_x$. For the $x = 0, 1$ and 4 compositions, in addition to the T_N , a low temperature anomaly is observed in the temperature range near 12 K (denoted as T_2 in the table). For the $x = 2$ and 3 compositions, we observe two more anomalies T_2 and T_3 in addition to the T_N . This points out that the magnetic structure and the low temperature magnetism of $\text{Mn}_2\text{SiS}_{4-x}\text{Se}_x$ compounds are more complex than the PM-AFM-WF transitions that were reported earlier.^{20,22,25} The presence of α -MnS found in two of the samples through x ray diffraction analysis does not influence the magnetism as α -MnS has a magnetic transition at $T = 140$ K but we do not observe any anomalies at this temperature in any of the compositions. The effective paramagnetic moment, μ_{eff} and the Curie-Weiss temperature, θ_{cw} are estimated from the inverse magnetic susceptibility versus temperature data following a curve-fit to Curie-Weiss law. The insets (1) and (2) in panel (b) shows the representative Curie-Weiss fits administered on Mn_2SiS_4 and Mn_2SiSe_4 as red solid lines. The estimated parameters from the fit are collected in Table II for all the five compositions. Slightly diminished values of effective moment compared to the theoretical spin-only moment of Mn^{2+} in d^5 state, $\mu_{\text{th}} = 5.92 \mu_B$, is observed in all the compounds except for Mn_2SiSe_4 . The Curie-Weiss temperature returns negative values which indicate that the overall magnetic interactions in these compounds are antiferromagnetic type. The frustration parameter, $f = \frac{|\theta_{cw}|}{T_N}$, shows a value of nearly 2.7 for all the compositions except for Mn_2SiSe_4 for which a higher value of 5.2 is recovered. This indicates that the compound Mn_2SiSe_4 is significantly frustrated than the other compounds. The frustration in $\text{Mn}_2\text{SiS}_{4-x}\text{Se}_x$ stems from the geometrical triangular saw-tooth like arrangement of Mn^{2+} spins. The value of f obtained for Mn_2SiS_4 compares well with the value reported for this material earlier²⁰. The magnetic frustration effect that is observed through the frustration index f is supported by the structural feature of the triangular Mn arrangement (refer Fig 1) that makes up the saw-tooth like lattice. In the case of Mn_2SiS_4 which has $f = 2.7$, the Mn-triangle has two equal distances, 3.97 Å and one 3.71 Å. However, in the case of Mn_2SiSe_4 which has a high f value (5.2), the Mn-triangle has all equal distance, 2.84 Å.

The magnetic structure of the $x = 0$ and 4 compounds, Mn_2SiS_4 and Mn_2SiSe_4 have been elucidated through neu-

tron powder diffraction methods.²³⁻²⁵ The neutron diffraction study of Mn_2SiS_4 confirmed the presence of olivine crystal structure in the whole temperature range of 4.2 K to 180 K. However, as noted previously, Mn in this structure occupies two distinct Wyckoff positions, 4a and 4c. At 4.2 K, the Mn moments in both the positions were found to be collinear with the y -axis. At higher temperature, the magnetic moment on the 4a site gradually rotates away from the y -axis. Between 83-86 K, both the 4a and 4c moments tend to align along the x -axis. However, the moments are subjected to canting in the x - z plane. A similar case of tendency for canting of the spins was observed in Mn_2SiSe_4 as well. However, in this case clear

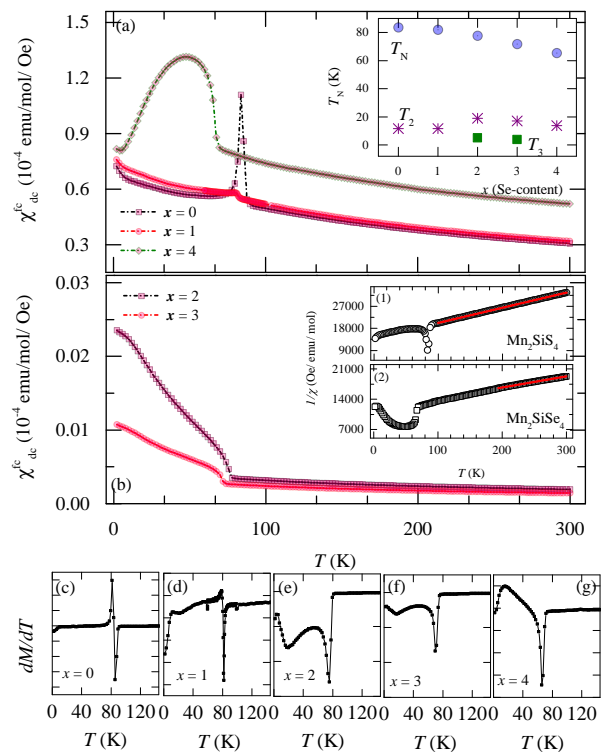


FIG. 4. (color online) The magnetic susceptibility of $\text{Mn}_2\text{SiS}_{4-x}\text{Se}_x$ ($x = 0-4$) obtained in 500 Oe field cooled condition presented for the $x = 0, 1, 4$ in panel (a) and $x = 2, 3$ in panel (b). The inset of panel (a) shows the T_N 's as a function of Se-content (x). The insets (1) and (2) in panel (b) shows the $1/\chi_{\text{dc}}^{\text{fc}}(T)$ curves of Mn_2SiS_4 and Mn_2SiSe_4 respectively along with Curie-Weiss fit (red solid line). (c-g) The derivative, dM/dT versus temperature showing the multiple anomalies present in each composition.

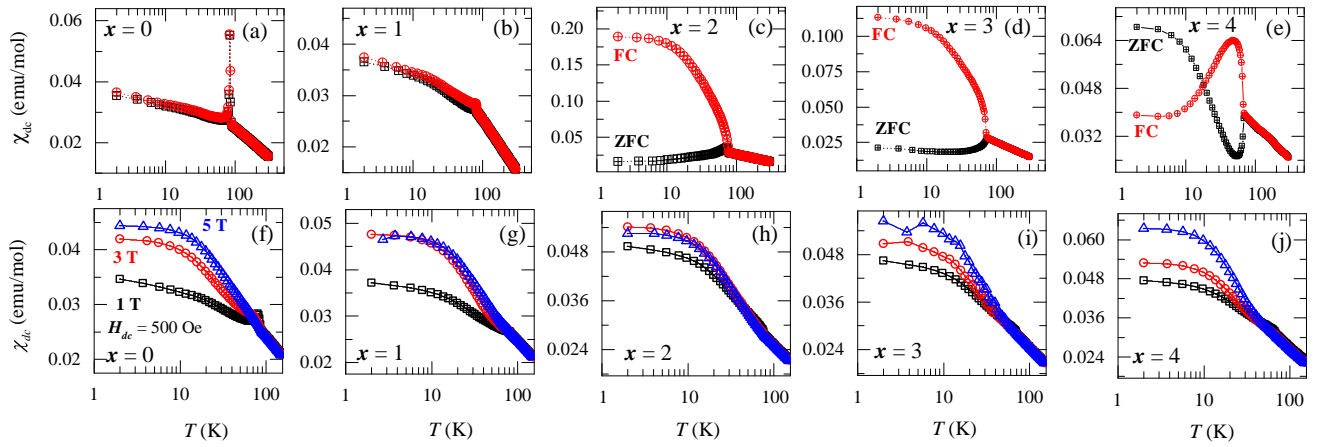


FIG. 5. (color online) (a-e) The dc magnetic susceptibility of $\text{Mn}_2\text{SiS}_{4-x}\text{Se}_x$ ($x = 0-4$) obtained in ZFC and FC protocol using an external field of 500 Oe. Large bifurcation in the ZFC and FC arms observed for $x = 2, 3$ whereas crossing of the ZFC and FC seen for $x = 4$. (f-j) Shows the dc susceptibility in field-cooled mode for 1 T, 3 T and 5 T for $x = 0-4$. Even with the application of 5 T, no significant enhancement of magnetic moment is obtained.

signature of diffuse magnetic scattering was observed, especially for the peaks at $2\theta = 22^\circ$ and 48° ²³. The magnetization of Mn_2SiSe_4 was then attributed to the short-range ferro or ferrimagnetic arrangement of canted spins. The spin correlations as a part of the diffuse magnetic scattering is seen to persist up to 102 K. The observation to diffuse magnetic scattering in Mn_2SiSe_4 from the previous studies support the frustrated magnetism observed through a high frustration index, f , and also low magnetic entropy released at the T_N .

Multiple magnetic phase transitions at low temperature were observed in Mn and Fe orthosilicate olivines.^{45,46} In $\text{Mn}_2\text{SiS}_{4-x}\text{Se}_x$ compounds, more than one magnetic anomaly is observed for all the compositions below their T_N (refer to Table II). By employing a Weiss mean-field model, the magnetic transitions in the Mn and Fe orthosilicates were qualitatively understood based on the parameter γ/α which is the ratio of the two superexchange angles present in the spin structure of these magnets. The ratio γ/α compares to the ratio, T_N/θ_{cw} . It was shown that in the special case where $2 < \gamma/\alpha < 1$, there arises a new low temperature phase transition below T_N and it is indicated by the low values of the ratio T_2/θ_{cw} where $T_2 < T_N$ is the low temperature transition. In Table II, we have collected the ratios T_N/θ_{cw} , T_2/θ_{cw} and T_3/θ_{cw} for the $\text{Mn}_2\text{SiS}_{4-x}\text{Se}_x$ compositions. It is easily noted that the value of T_N/θ_{cw} is relatively constant across the compositions, except for the highly frustrated composition, Mn_2SiSe_4 . Also, the values of T_2/θ_{cw} and T_3/θ_{cw} are highly diminished compared to that of T_N/θ_{cw} . This is in agreement with the simple Weiss-field approach where the calculated exchange energies supported the low temperature magnetic anomalies. The broadness of the magnetic anomalies below T_N in the Mn_2SiSe_4 compositions point toward short-range magnetic order rather than a long-range magnetic order in to a new magnetic structure. The dc magnetic susceptibility of the $\text{Mn}_2\text{SiS}_{4-x}\text{Se}_x$ series in zero field-cooled (ZFC) and field-cooled (FC) protocol in the presence of external magnetic field, $H_{app} = 500$ Oe is presented in Fig 5

(a-e). The effect of an external magnetic fields 1 T, 3 T and 5 T upon the field-cooled magnetic susceptibility is shown in the panels (f-j) of the same figure. For the compositions $x = 0, 1$, the ZFC and the FC arms show no bifurcation at all (a, b). The magnetic phase transition is evident as a strong anomaly thereby confirming the AFM transition. For the compositions $x = 2, 3$, and 4 strong irreversibilities are observed in the magnetic response which is an indication of significant short-range magnetic correlations or spin glass-like features. Interestingly, the highly frustrated compound Mn_2SiSe_4 presents a ZFC/FC response where the ZFC and FC arms cross each other in the low temperature region. This crossing happens at $T \approx 18$ K. This feature resembles the case of negative magnetization observed in many other oxide systems.⁴⁷⁻⁴⁹ In the case of the spinel compound Co_2VO_4 , the negative magnetization was explained in terms of a ferrimagnetic structure ($T_c = 158$ K) and the resulting complex magnetism at low temperature. However, the presence of ferromagnetic clusters embedded in an AFM matrix also can display negative magnetization as evidenced in the case of the rare-earth manganite, $\text{NdMnO}_{3\pm\delta}$ where the stoichiometry of the oxygens also seem to play a role.⁴⁸ In order to accurately determine the presence of ferromagnetic short-range ordered clusters, low temperature neutron diffraction experiments were undertaken. In the case of Mn_2SiSe_4 , the magnetic structure that is proposed already point towards the presence of short-range ferro or ferrimagnetic arrangement of canted spins. The magnetization data presented in Fig 5 (e) supports the claim of short-range ferrimagnetic canted spins. However, a detailed low temperature neutron powder diffraction study can shed more light on the proposed magnetic features. It can be noted that the application of external magnetic fields up to 5 T does not produce appreciable enhancement of the magnetization in any of the $\text{Mn}_2\text{SiS}_{4-x}\text{Se}_x$ compositions (panels (f-j)).

The magnetization data presented in Fig 4 and Fig 5 clearly support a scenario of short-range magnetic order related to the spin fluctuations in the antiferromagnetic state. Though

there is a definite role played by geometric frustration on the saw-tooth lattice, it can be understood that magnetic anisotropy is also a key parameter that needs to be taken into account. Strong anisotropy effects in the magnetic response have been reported in single crystals of Mn_2SiS_4 evidenced by the metamagnetic-like spin flop transition²⁰. Notably, the spin flop critical field was found to decrease and vanish at the antiferromagnetic transition temperature in the case of Mn_2SiS_4 . The present study, that is performed on polycrystalline samples, reveal the metamagnetic-like features in magnetization isotherms, thereby underlining the importance of anisotropy. Detailed torque magnetometry studies on single crystals of low dimensional magnets have revealed the magnetocrystalline anisotropy effects in spin reorientation⁵⁰. The $S = 1/2$ saw-tooth chain in $\text{Cu}_2\text{Cl}(\text{OH})_3$ is a recent example of a similar lattice where anisotropy effects were observed in magnetization and magnetostriction, under the application of high magnetic fields⁵¹.

The isothermal magnetization curves, $M(H)$, as a function of applied field H in the range -7 T to $+7$ T at 2 K for $\text{Mn}_2\text{SiS}_{4-x}\text{Se}_x$ $x = 0 - 4$ are plotted together in Fig 6 (a). The curves represent typical antiferromagnetic response with no indication of magnetic hysteresis. At 2 K and 7 T, the maximum magnetic moment attained is about $0.77 \mu_B/\text{f.u.}$ for Mn_2SiSe_4 . The lowest moment is attained for Mn_2SiS_4 which has a value of $0.55 \mu_B/\text{f.u.}$ One of the earliest work on the Mn-chalcogenide olivines was related to the spin-flop transition and the associated tricritical point in the H - T phase diagram.²⁰ The field-induced spin-flop transitions are reproduced in all the compositions in the present series of Mn_2SiSe_4 ($x = 0-4$). The field-induced spin-flop transitions are clearly evidenced in the derivatives dM/dH versus $H(T)$ plotted in Fig 6 (b-d) which are shown for $x = 0, 2$ and 4. The

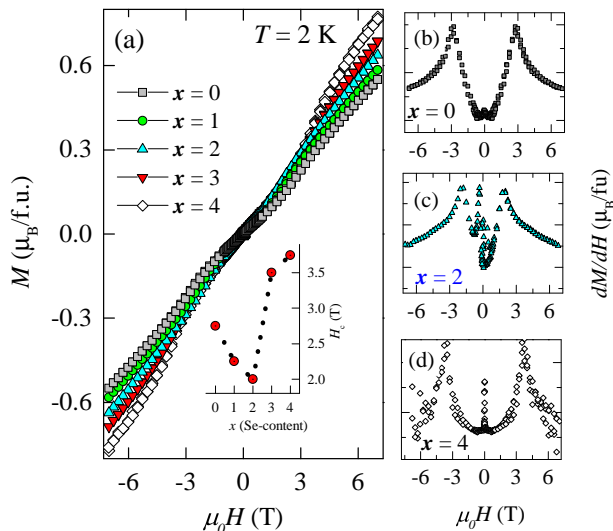


FIG. 6. (color online) (a) The isothermal magnetization of $\text{Mn}_2\text{SiS}_{4-x}\text{Se}_x$ ($x = 0-4$) at 2 K. The inset shows the evolution of the critical field, H_c , as a function of Se content, x . (b-d) The derivative, dM/dH versus temperature showing the presence of metamagnetic phase transitions.

variation of the critical field H_c for spin-flop as a function of the Se-content is presented in the inset of (a). The spin-flop transition in Mn_2SiS_4 single crystals along the crystallographic c -axis is observed at a critical field of about 3 T. In the present case, our samples of polycrystalline Mn_2SiS_4 also display the spin-flop transition at a comparable field value of 2.7 T. It can be observed that the H_c first decreases with the replacement of S with Se, until $x = 2$. Beyond $x = 2$, for $x = 3, 4$ H_c increases and reaches a maximum for Mn_2SiSe_4 which is in fact, the highly frustrated composition in this group. In order to correlate the crystal and the electronic structure of the $\text{Mn}_2\text{SiS}_{4-x}\text{Se}_x$ and to explore the band structure peculiarities of the current compositions as compared to that observed in Fe-based olivines that are predicted thermoelectrics¹⁸, we now take a look at the results from density functional theory calculations.

D. Density functional theory and thermal conductivity

The magnetic structure of Mn_2SiS_4 and Mn_2SiSe_4 are reported in the antiferromagnetic structure through neutron diffraction studies^{23,24}. The magnetic moments of Mn are proposed to lie in the c direction; the spins in the ab plane are ferromagnetically coupled while the adjacent layers are coupled antiferromagnetic. We have performed the DFT calculations for the antiferromagnetic spin arrangement of the four different compositions in $\text{Mn}_2\text{SiS}_{4-x}\text{Se}_x$. The experimental crystal structure for Mn_2SiS_4 , obtained from the room temperature structure determined in the present work, was used as the starting point to generate the initial structures for all the four compounds following a energy-minimization process. The crystal symmetry is found to be orthorhombic with six inequivalent positions, agreeing with the $Pbnm$ space group reported⁴¹. The optimized lattice constants, spin magnetic moments, and the band gaps of these systems are summarized in Table III and presented along with the corresponding experimental values for easy comparison. The total energy with the optimized lattice constants is lower than that with experimental lattice constants by 0.4 eV. The calculated magnetic moments on the Mn atoms show antiferromagnetic spin ordering. The DFT-calculated magnetic structure was found to match the experimental structure reported through previous neutron diffraction experiments²⁴. The range of the calculated spin magnetic moments, μ_c , are presented in the table for the optimized structure. An agreement is found between the μ_c and the experimental values (μ_t) obtained from magnetization results of the present work. The substitution of one S by Se leads to two structures with the formula unit of $\text{Mn}_2\text{SiS}_3\text{Se}$ which are identified as structures (a) and (b) in Table III. Similar substitution by two Se atoms also leads to two structures using the same set of inequivalent atom positions. Apart from these, we also tested mixed structures with random substitutional positions in a supercell which led to $\text{Mn}_2\text{SiS}_3\text{Se}$ and $\text{Mn}_2\text{SiS}_2\text{Se}_2$ based on atom count only. However, we find that some of these structures have lower energy than the structures that conform to the orthorhombic symmetry and therefore we include them

TABLE III. The total energy (E_{AFM}), theoretical and experimental lattice parameters ($(a, b, c)_{th}$ and $(a, b, c)_{exp}$) magnetic moments (μ_t/Mn and μ_c/Mn) and the calculated band gaps from the DFT calculations.

Composition	E_{AFM} (eV)	$(a, b, c)_{th}$ (Å)	$(a, b, c)_{exp}$ (Å)	μ_c/Mn (μ_B)	μ_t/Mn (μ_B)	Δ_b (eV)
Mn_2SiS_4	0.0	12.46, 7.27, 5.87	12.69, 7.44, 5.94	4.04, -4.05	4.0	0.47
	0.40	12.69, 7.44, 5.94		4.12, -4.16		0.64
Mn_2SiS_3Se (a)	0.34	12.726, 7.320, 5.892	12.860, 7.527, 6.009	4.03, -4.03	4.07	
Mn_2SiS_3Se (b)	0.35	12.530, 7.315, 6.013		4.04, -4.04		0.40
Mn_2SiS_3Se (1)	0.0	12.59, 7.35, 5.91		4.02, -4.02		0.32
Mn_2SiS_3Se (2)	0.02	12.583, 7.335, 5.942		4.02, -4.03		
Mn_2SiS_3Se (3)	0.12	12.590, 7.34, 5.96		4.04, -4.02		
Mn_2SiS_3Se (4)	0.10	12.603, 7.338, 5.915		4.02, -4.03		
$Mn_2SiS_2Se_2$	0.0	12.538, 7.432, 5.893	13.00, 7.61, 6.08	3.97, -3.97	3.95	
Mn_2SiSSe_3	0.0	12.75, 7.45, 5.92	13.150, 7.690, 6.156	3.92, -3.92	3.8	0.1
Mn_2SiSe_4	0.0		13.30, 7.78, 6.24	4.12, -4.12	5.9	0.45

in the results, identified as structures Mn_2SiS_3Se (1)-(4) in the Table III. For the $Mn_2SiS_2Se_2$ compound, substitution of inequivalent atoms leads to the lowest energy structure compared to random substitution and therefore we present only the lowest energy structure in the table. However, for this compound and for Mn_2SiSSe_3 , random substitution can lead to low lying structures within 0.02–0.07 eV above the ground state. The Mn_2SiSe_4 compound with experimental lattice parameters is the lowest energy structure. For all the five compounds studied, the antiferromagnetic phase is the stable magnetic phase. The trend of the spin moment of the mixed compounds compare excellently with the trend seen from experiment. With higher number of Se atoms in the mixed compound, the spin moment decreases. However, the spin moment of the Mn_2SiSe_4 from DFT is much smaller compared to that derived from experimental data. We find that there can be several local minima in the potential energy surface with slightly different lattice constants for this compound. In all cases however the spin moment is still smaller than the experimental value. The experimental spin moments are determined from magnetization data collected at elevated temperatures where lattice expansion can lead to reduced interactions between atoms. The DFT calculations are done without any temperature effect which may explain the difference between the DFT and experimental spin moments. Moreover, these calculations also do not take into account non-collinear spin moments.

The band structure of the two terminal compounds Mn_2SiS_4 and Mn_2SiSe_4 are shown in Fig 7 (a, b) respectively. The bandgap of Mn_2SiS_4 and Mn_2SiSe_4 was found to be 0.47 eV and 0.45 eV respectively. Both structures have a direct bandgap as indicated by the valence band maximum (VBM) and conduction band maximum (CBM) from the band structure plot. The band structures have flat bands from G-X crystallographic direction and similar to that of Gudelli *et al.*¹⁸ in their Fe_2GeS_4 and Fe_2GeSe_4 band structure plots. The corresponding total and projected density of states (DOS) for Mn_2SiS_4 and Mn_2SiSe_4 are represented in panels (c, d) of Fig 7. The DOS shows that the states near the Fermi level arise mainly from the Mn d-states and S/Se p states. In both the system the Si states lie deeper in energy. The conduction band has contribution mainly from the Mn d states. The

band gap obtained in the present study differ from those reported for Mn_2SiS_4 ⁵². However, the antiferromagnetic spin arrangement assumed in the work by Davydova *et al* seem to be different from the AFM structure that is obtained in the present work as well as in earlier neutron reports²⁴.

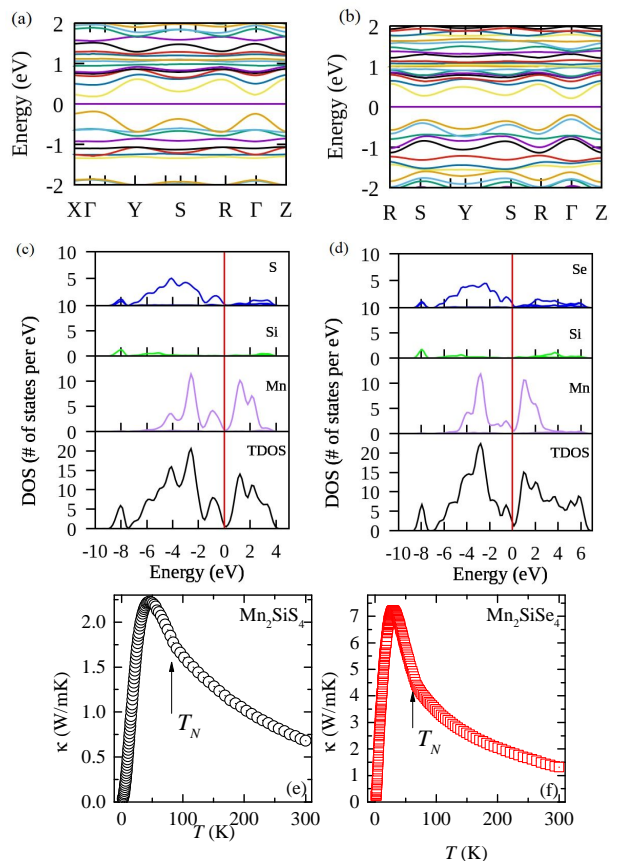


FIG. 7. (color online) The DFT predicted band structure of (a) Mn_2SiS_4 and (b) Mn_2SiSe_4 . The electronic projected density of states (PDOS) for Mn_2SiS_4 and Mn_2SiSe_4 are shown in (c) and (d) respectively. The experimentally measured thermal conductivity of (e) Mn_2SiS_4 and (f) Mn_2SiSe_4 . The arrows mark the temperature of antiferromagnetic phase transition.

An LDA + U approach was used by Davydova *et al* which influences the band gap since U can be adjusted to match the experimental band gap.

Motivated by the band structure features that we found in Mn_2SiS_4 and Mn_2SiSe_4 and from the reports on other thio-olivines that project these materials as potential candidates for thermoelectric applications, we measured the thermal conductivity, $\kappa(T)$. Figure 7 (e, f) shows the $\kappa(T)$ for Mn_2SiS_4 and Mn_2SiSe_4 respectively. Both compounds show thermal conductivity that is reminiscent of semiconducting materials where phonons dominate the thermal transport⁵³. At low temperatures the thermal conductivity rapidly increases with increasing temperature, forms a pronounced maximum centered below 50 K, and then decreases down to room temperature. The maximum in low temperatures occurs due to reduction of the thermal scattering at low temperatures, i.e., in the regime where the phonon mean free path becomes larger than the interatomic distances. For both compounds the magnetic phase transition appears only as a small kink in $\kappa(T)$ at the Néel temperature (marked by arrows in Fig 7 (e, f)). The band gap obtained for Mn_2SiSe_4 is slightly diminished compared to that of Mn_2SiS_4 and the former shows *p*-type conductivity according to our Seebeck coefficient measurement (not shown).

As the Se-content is increased from $x = 0$ to $x = 4$, the sharp magnetic transition observed in Mn_2SiS_4 is replaced with a broad transition extending over a large temperature range below 65 K. The results of magnetization and the specific heat experiments point towards the emergence of short-range order stemming from enhanced magnetic frustration. In Fig 8 the Mn-Mn distances between the Mn atoms occupying the crystallographically distinct m_1 and m_2 positions are represented for Mn_2SiS_4 , $\text{Mn}_2\text{SiS}_2\text{Se}_2$ and Mn_2SiSe_4 . The distances marked on the figure are obtained from the refined x-ray diffraction data which is cross-checked against the distances obtained from DFT. It can be seen from the figure that the Mn-triangles that form the saw-tooth lattice are isosceles and the Mn-Mn distances between the atoms in the m_1 chain (along *b*) increases with Se-content. In general, the distances in the Mn-triangle increases from Mn_2SiS_4 towards Mn_2SiSe_4 . The Mn(m_1)–Mn(m_1) distance along the *c*-direction for Mn_2SiS_4 is 5.94 Å which increases to 6.24 Å for Mn_2SiSe_4 . The Mn(m_1)–Mn(m_1) distances also undergo a similar increase. From this, it is clear that the inter-layer distance between the saw-tooth layers increase towards Mn_2SiSe_4 and subsequently a weakening of the exchange interaction can result. These structural features associated with the saw-tooth triangles lead to the formation of spin clusters in $\text{Mn}_2\text{SiS}_{4-x}\text{Se}_x$ with increased Se-content resulting in predominant short-range order.

IV. CONCLUSIONS

The magnetism of chalcogenide olivine $\text{Mn}_2\text{SiS}_{4-x}\text{Se}_x$ with a saw-tooth lattice for the Mn moments are studied in detail using magnetization, specific heat and first-principles

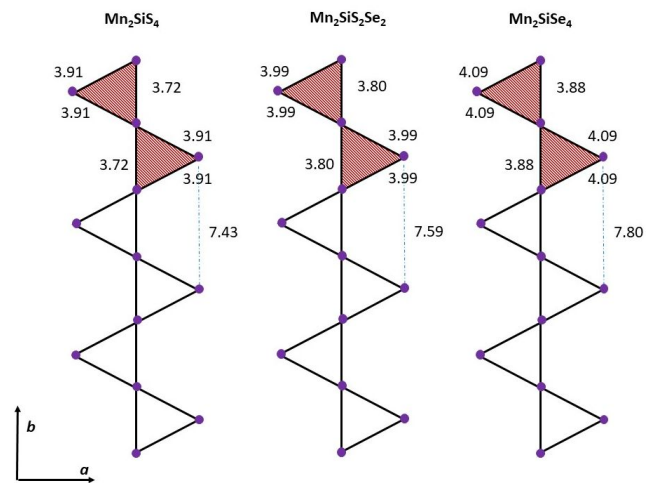


FIG. 8. (color online) A schematic figure showing the saw-tooth chain of Mn in Mn_2SiS_4 , $\text{Mn}_2\text{SiS}_2\text{Se}_2$ and Mn_2SiSe_4 . The distance between Mn in m_1 and m_2 positions are marked. The Mn-triangles tend to form isosceles in all the $\text{Mn}_2\text{SiS}_{4-x}\text{Se}_x$ compositions. The distance between the 2-triangle units (shaded region) along *b*-direction increases as the Se-content increases. The inter-layer distances between the saw-tooth layers (in *ab*-plane) also increases with higher Se-content.

density functional theory calculations. Progressive substitution of S using Se in Mn_2SiS_4 is seen to shift the antiferromagnetic transition temperature from 86 K to 66 K. Though an antiferromagnetic transition is clear, the magnetic entropy estimated from the analysis of specific heat reveals diminished values suggesting strong spin fluctuations present. Among the $\text{Mn}_2\text{SiS}_{4-x}\text{Se}_x$ compositions studied, Mn_2SiSe_4 is the most frustrated. A non-linear trend in the evolution of the critical field for spin-flop is found across the compositions. Density functional theory calculations support the stable orthorhombic crystal structure across the series and confirms the antiferromagnetic structure for Mn_2SiS_4 and Mn_2SiSe_4 . Quasi-flat-band features similar to that seen in Fe-based olivines are seen in the present case however, the experimental thermal transport results do not support features favourable for a good thermoelectric.

V. ACKNOWLEDGEMENTS

HSN acknowledges the UTEP start-up fund and UT Rising-STAR in supporting this work. BS acknowledges the financial support for this work provided by the University of Oklahoma startup funds. DA and KG acknowledge support from DOE's (Basic Energy Science) Early Career Research Program. RRZ and TB acknowledge support by Department of Energy Basic Energy Science through Grant Nos. DESC0002168 and DESC0006818. Support for computational time by the NSF's XSEDE project through grant TGDMR090071 is gracefully acknowledged. AC and SRS acknowledge The University of Texas at El Paso (UTEP) Start-up fund and NSF-PREM Program (DMR1205302). The part of the paper prepared by

Dr. Singamaneni and co-author A. Cosio are funded under the Award No. 31310018M0019 from UTEP, Nuclear Regulatory Commission. The statements, findings, conclusions,

and recommendations are those of the author(s) and do not necessarily reflect the view of the UTEP or The US Nuclear Regulatory Commission.

-
- * saparov@ou.edu
† hnair@utep.edu
- ¹ K. Kubo, Phys. Rev. B **48**, 10552 (1993).
 - ² D. Sen, B. S. Shastry, R. Walstedt, and R. Cava, Phys. Rev. B **53**, 6401 (1996).
 - ³ T. Nakamura, Phys. Rev. B **53**, 6393 (1996).
 - ⁴ S. Blundell and M. Núñez-Regueiro, Eur. Phys. J. B **31**, 453 (2003).
 - ⁵ V. Ohanyan, Condens. Matter Phys. **12**, 343 (2009).
 - ⁶ S. Bellucci and V. Ohanyan, Eur. Phys. J. B **75**, 531 (2010).
 - ⁷ Z. Hao, Y. Wan, I. Rousochatzakis, J. Wildeboer, A. Seidel, F. Mila, O. Tchernyshyov, et al., Phys. Rev. B **84**, 094452 (2011).
 - ⁸ V. Chandra and D. Sen, Phys. Rev. B **69**, 214406 (2004).
 - ⁹ M. Zhitomirsky, Phys. Rev. B **70**, 100403 (2004).
 - ¹⁰ M. Zhitomirsky, Prog. Theor. Phys. Suppl. **160**, 361 (2005).
 - ¹¹ X. Wang, H. Zhang, and X. Wang, Phys. Rev. Appl. **9**, 024029 (2018).
 - ¹² R. Cava, J. Solid State Chem. **104**, 437 (1993).
 - ¹³ O. Le Bacq, Phys. Rev. B **71**, 014432 (2005).
 - ¹⁴ G. Lau, Phys. Rev. B **73**, 012413 (2006).
 - ¹⁵ J. White, T. Honda, K. Kimura, T. Kimura, C. Niedermayer, O. Zaharko, A. Poole, B. Roessli, and M. Kenzelmann, Phys. Rev. Lett. **108**, 077204 (2012).
 - ¹⁶ S. J. Fredrick and A. L. Prieto, J. Amer. Chem. Soc. **135**, 18256 (2013).
 - ¹⁷ J. K. Furdyna and J. Kossut, *Diluted magnetic semiconductors, semiconductors and semimetals (eds) RK Willardson and AC Beer* (New York: Academic Press, 1988).
 - ¹⁸ V. K. Gudelli, V. Kanchana, and G. Vaitheeswaran, J. Phys.: Condens. Matter **28**, 025502 (2015).
 - ¹⁹ I. S. Hagemann, P. G. Khalifah, A. P. Ramirez, and R. J. Cava, Phys. Rev. B **62**, R771 (2000).
 - ²⁰ K. Ohgushi and Y. Ueda, Phys. Rev. Lett. **95**, 217202 (2005).
 - ²¹ G. Lamarche, F. Lamarche, and A.-M. Lamarche, Physica B **194**, 219 (1994).
 - ²² S. Jobic, F. Bode, P. Le Boterf, and G. Ouvrard, J. Alloys and Comp. **230**, 16 (1995).
 - ²³ F. Bodenan, V. B. Cajipe, G. Ouvrard, and G. Andre, J. Magn. Magn. Mater. **164**, 233 (1996).
 - ²⁴ A.-M. Lamarche, G. Lamarche, C. Church, J. C. Woolley, I. P. Swainson, and T. M. Holden, J. Magn. Magn. Mater. **137**, 305 (1994).
 - ²⁵ A. Junod, K.-Q. Wang, G. Triscone, and G. Lamarche, Journal of magnetism and magnetic materials **146**, 21 (1995).
 - ²⁶ B. I. Park, S. Yu, Y. Hwang, S. H. Cho, J. S. Lee, C. Park, D. K. Lee, and S. Y. Lee, J. Mater. Chem. A **3**, 2265 (2015).
 - ²⁷ H. A. Platt, *Copper and iron chalcogenides for efficient solar absorption* (Oregon State University, 2010).
 - ²⁸ K. Momma and F. Izumi, J. Appl. Crystallogr. **44**, 1272 (2011).
 - ²⁹ G. Kresse and J. Hafner, Phys. Rev. B **47**, 558 (1993).
 - ³⁰ J. Furthmüller, J. Hafner, and G. Kresse, Phys. Rev. B **50**, 15606 (1994).
 - ³¹ G. Kresse and J. Furthmüller, Comp. Mater. Sci. **6**, 15 (1996).
 - ³² G. Kresse and J. Furthmüller, Phys. Rev. B **54**, 11169 (1996).
 - ³³ P. E. Blöchl, Phys. Rev. B **50**, 17953 (1994).
 - ³⁴ G. Kresse and D. Joubert, Phys. Rev. B **59**, 1758 (1999).
 - ³⁵ P. E. Blöchl, C. J. Först, and J. Schimpl, Bull. Mater. Sci. **26**, 33 (2003).
 - ³⁶ J. P. Perdew, K. Burke, and M. Ernzerhof, Phys. Rev. Lett. **77**, 3865 (1996).
 - ³⁷ H. J. Monkhorst and J. D. Pack, Phys. Rev. B **13**, 5188 (1976).
 - ³⁸ A. Choudhury, S. Strobel, B. R. Martin, A. L. Karst, and P. K. Dorhout, Inorg. Chem. **46**, 2017 (2007).
 - ³⁹ J. C. Flanagan and M. Shim, The Journal of Physical Chemistry C **119**, 20162 (2015).
 - ⁴⁰ A. de Kergommeaux, J. Faure-Vincent, A. Pron, R. de Bettignies, B. Malaman, and P. Reiss, J. Amer. Chem. Soc. **134**, 11659 (2012).
 - ⁴¹ J. Fuhrmann and J. Pickardt, Acta Crystallogr. C **45**, 1808 (1989).
 - ⁴² K. Ohgushi and Y. Ueda, in *AIP Conference Proceedings* (AIP, 2006), vol. 850, pp. 1277–1278.
 - ⁴³ K. Ohgushi and Y. Ueda, J. Magn. Magn. Mater. **310**, 1291 (2007).
 - ⁴⁴ R. t. Shannon and C. Prewitt, Acta Crystallogr. B **26**, 1046 (1970).
 - ⁴⁵ H. Kondo and S. Mlyahara, J. Phys. Soc. Jpn. **21**, 2193 (1966).
 - ⁴⁶ R. Santoro, R. Newnham, and S. Nomura, J. Phys. Chem. Solids **27**, 655 (1966).
 - ⁴⁷ A. Kumar and S. Yusuf, Phys. Rep. **556**, 1 (2015).
 - ⁴⁸ F. Bartolomé, J. Bartolomé, and J. Campo, Physica B **312**, 769 (2002).
 - ⁴⁹ N. Menyuk, K. Dwight, and D. Wickham, Phys. Rev. Lett. **4**, 119 (1960).
 - ⁵⁰ N. Novosel, W. Lafargue-Dit-Hauret, Ž. Rapljenović, M. Dragičević, H. Berger, D. Cinčić, X. Rocquefelte, and M. Herak, Phys. Rev. B **99**, 014434 (2019).
 - ⁵¹ L. Heinze, H. Jeschke, A. Metavitsiadis, M. Reehuis, R. Feyherm, J.-U. Hoffmann, A. Wolter, X. Ding, V. Zapf, C. Moya, et al., arXiv preprint arXiv:1904.07820 (2019).
 - ⁵² A. Davydova, J. Eriksson, R. Chen, K. Rudisch, C. Persson, and J. J. S. Scragg, Materials & Design **152**, 110 (2018).
 - ⁵³ T. M. Tritt, *Thermal conductivity: theory, properties, and applications* (Springer Science & Business Media, 2005).